ACS Catalysis

Research Article

pubs.acs.org/acscatalysis

In Situ Loading Transition Metal Oxide Clusters on TiO_2 Nanosheets As Co-catalysts for Exceptional High Photoactivity

Lichen Liu,[†,‡] Zeyang Ji,[†,‡] Weixin Zou,[†,‡] Xianrui Gu,[†,‡] Yu Deng,[‡] Fei Gao,[‡] Changjin Tang,*[,†,‡] and Lin Dong*[,†,‡]

[†]Key Laboratory of Mesoscopic Chemistry of Ministry of Education, School of Chemistry and Chemical Engineering and [‡]Jiangsu Key Laboratory of Vehicle Emissions Control, Center of Modern Analysis, Nanjing University, Nanjing 210093, PR China

Supporting Information

ABSTRACT: In this work, transition metal oxide clusters (MnO_x, FeO_x, CoO_x, NiO_x, and CuO_x, denoted as TM-TiO_2) are *in situ* loaded on TiO_2 nanosheets through one-pot reaction. Structural and pore structural characterizations prove that metal ions do not dope into the frameworks of TiO_2 nanosheets. Through TEM and STEM, we can determine that clusters with ~2 nm size are finely dispersed on TiO_2 nanosheets. PL spectra and photoelectrochemical measurements suggest that these metal oxide clusters can serve as hole traps. Time-resolved PL spectra demonstrate that the charge-transfer process in TM-TiO_2 is significantly accelerated, leading to higher charge separation efficiency. Metal oxide clusters show significant promotion effect in photocatalytic water oxidation to O_2 compared to RuO_2/TiO_2 and IrO_2/TiO_2 nanosheets (denoted as Ru-TiO_2(IM) and Ir-TiO_2(IM)) prepared through conventional impregnation method. We also prepared RuO_2/TiO_2 and Ir/TiO_2 nanosheets (denoted as Ru-TiO_2(HT) and Ir-TiO_2(HT)) through the *in situ* loading method. Ru-TiO_2(HT) and Ir-TiO_2(HT) show O_2 evolution rates much better than those of Ru-TiO_2(IM) and Ir-TiO_2(IM) due to the smaller sizes of RuO_2 and IrO_2. However, Mn-TiO_2 and Co-TiO_2 still display better photoactivities compared to those of Ru-TiO_2(HT) and Ir-TiO_2(HT). These results indicate that transition metal oxides with small sizes can also work as co-catalysts in photocatalysis to substitute noble metal oxides.

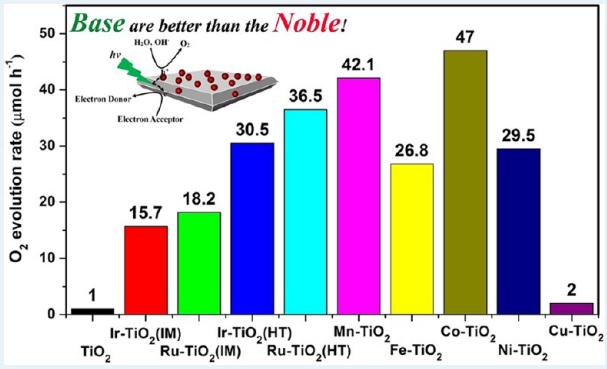

KEYWORDS: *metal oxide clusters, interfacial charge transfer, heterojunctions, photocatalytic O_2 evolution, TiO_2 nanosheets*

INTRODUCTION

TiO_2, as the most widely used semiconductor in photocatalysis and solar energy conversion, has distinguished advantages: low cost, high stability, and environmental friendliness.[1,2] However, the disadvantages of nanocrystalline TiO_2 are also conspicuous: low absorbance of visible light, fast recombination of photogenerated electrons and holes, and exposure of low activity crystal facets in conventional TiO_2-based materials. Much effort has been made to improve the response of TiO_2 to visible light, and great progress has been made. By doping nonmetallic or metallic elements, we can introduce a dopant energy level in the band gap of TiO_2, leading to visible-light response.[3,4] Besides, coupling TiO_2 with dye molecules or narrow-band gap semiconductors is also an alternative strategy to obtain excellent TiO_2-based photocatalytic materials under visible light.[5,6] Despite the advances in synthesizing visible-light TiO_2-based photocatalysts, improving the charge separation efficiency in TiO_2 still remains a great challenge. As a result of the fast recombination of photogenerated electrons and holes, most of the excited charge carriers are quenched before they can reach the surface to participate photocatalysis reaction. Thus, it is important to develop practical methods to improve the charge separation efficiency in TiO_2 photocatalytic materials.[7] On the basis of the present research, building heterojunctions on TiO_2 is the one of the most effective approaches to overcome this problem.[8] The photogenerated electrons and holes can be separated by the electrical field at the interface of different semiconductors, resulting in the separation of electrons and holes.

Generally, there are two methods to enhance the efficiency of charge separation in TiO_2-based photocatalytic materials: loading noble metal nanoparticles or depositing noble metal oxide nanoparticles as co-catalysts.[9,10] Although some other co-catalysts such as cobalt phosphate can also show superior performance, these two methods are the most widely used in previous studies. After loading metal nanoparticles (Pt, Au, etc.) on TiO_2, a metal-semiconductor Schottky or Ohmic barrier will form, and the metal nanoparticles will serve as a trap for excited electrons.[11−13] In addition, metal oxides also can serve as traps for excited electrons.[14] Another method is to employ noble metal oxide nanoparticles (RuO_2, IrO_2, etc.) as the co-catalysts for trapping photogenerated holes.[15] Various

Received: April 12, 2013
Revised: July 24, 2013
Published: July 26, 2013

studies have proved that these two strategies are quite effective to promote the charge separation efficiency in photocatalysis.[16] However, it is quite expensive to use these noble metal or metal oxides as co-catalysts for industrial photocatalytic applications. Therefore, it is of great benefit to exploit cheap, earth-abundant metals (or metal oxides) as co-catalysts.

Recently, researchers have turned to transition metal oxides as the substitutes of noble metal oxides.[17] Long et al. have synthesized cobalt-modified $BiVO_4$ for the photocatalytic degradation of phenol. The CoO_x nanoparticles are supported on $BiVO_4$ to form p-n junctions between CoO_x and $BiVO_4$, which improve the charge separation efficiency.[18] Zhang et al. synthesized cobalt-modified porous single-crystalline $LaTiO_2N$ for water oxidation to O_2. In this work, CoO_x nanoparticles are deposited on the surface of $LaTiO_2N$ as the center for enrichment of holes, which show significantly higher performance than conventional IrO_2 nanoparticles.[19] In addition to CoO_x, NiO_x also can serve as the co-catalyst to promote the separation of electron−hole pair. Osterloh et al. have demonstrated that the $NiO_x/SrTiO_3$ nanocomposites show excellent activity in photo-oxidation of water.[20] And the mechanism proposed by Frank E. Osterloh[21] shows that NiO_x particles are the hole traps for water oxidation to O_2. In these above works, the modified metal oxide nanoparticles are almost larger than 5 nm. As we know, the interface charge transfer rate shows great dependence on the size of the particle. When the heterojunctions are as small as 2−3 nm, the charge transfer will be quite fast, leading to higher electron−hole separation efficiency.[7,22] Thus, it is of great importance to develop for loading ultrasmall metal oxide nanoparticles (∼2 nm) on semiconductor photocatalysts (e.g., TiO_2) as co-catalysts for enhanced charge separation efficiency.

In this work, we present a general strategy for *in situ* loading ultrasmall metal oxide nanoparticles on TiO_2 nanosheets with active {001} facets exposed. A series of metal oxide nanoparticles (MnO_x, FeO_x, CoO_x, NiO_x, CuO_x) with ultrasmall sizes (∼2 nm) are loaded on TiO_2 nanosheets to promote electron−hole separation in TiO_2 nanosheets. The photocatalytic O_2 evolution from water oxidation is employed as the probe reaction to evaluate the performances of these metal oxide nanoparticle/TiO_2 nanosheets (denoted as TM-TiO_2, TM=Mn, Fe, Co, Ni and Cu). The photocatalytic tests show that the as-prepared TM-TiO_2 samples are more active than RuO_2/TiO_2 and IrO_2/TiO_2 nanosheets (denoted as Ru-TiO_2 and Ir-TiO_2), which suggests that transition metal oxides nanoparticles may also work as the highly efficient co-catalysts for photocatalysis. This finding may contribute to build more economic and high-performance photocatalyst.

EXPERIMENTAL SECTION

Synthesis of Metal Oxide Clusters Modified TiO_2 Nanosheets (TM-TiO_2 Nanosheets). In the typical procedure for the synthesis of TM-TiO_2 nanosheets, a given amount of metal precursor (the details are summarized in Supplementary Table S1) was dissolved into 25 mL of $Ti(OBu)_4$ (TBOT) under stirring for 24 h; afterward, a colorful solution would be formed. Then 3 mL of hydrofluoric acid solution (40 wt %) was dropped to the above solution under strong stirring. After the addition of HF, stirring was continued for 1−2 h until the mixture changed into gel. The gel was transferred into a dried Teflon autoclave with a capacity of 50 mL and then kept at 180 °C for 36 h. After being cooled to room temperature, the powder was separated by high-speed centrifugation and washed with ethanol and distilled water several times. At last, these products were dried in an electric oven under air flow at 110 °C for 8 h. The obtained power was washed with hot water (∼80 °C) to remove the absorbed metal salts on the surface of TiO_2 nanosheets. In order to obtain F-free TM-TiO_2 nanosheets, 1.0 g of power was dispersed in 0.1 M NaOH aqueous and stirred for 8 h at room temperature. The power was recovered by high-speed centrifugation, washed with distilled water and ethanol several times to neutral, and then dried at 80 °C for 6 h.

Synthesis of Pure TiO_2 Nanosheets (TiO_2 Nanosheets). Pure TiO_2 nanosheets were prepared by the hydrothermal method reported by Xie et al.,[23] which is similar to that of TM-TiO_2 nanosheets. In a typical experimental procedure, 25 mL of $Ti(OBu)_4$ (TBOT) and 3 mL of hydrofluoric acid solution (40 wt %) were mixed in a dried Teflon autoclave with a capacity of 100 mL and then kept at 180 °C for 36 h. After being cooled to room temperature, the white powder was separated by high-speed centrifugation and washed with ethanol and distilled water several times. At last, these products were dried in an electric oven under air flow at 80 °C for 6 h. The hydrothermal product was also washed with 0.1 M NaOH aqueous to remove fluorine as described in the synthesis of TM-TiO_2 nanosheets.

Ru-TiO_2 and Ir-TiO_2 nanosheets are prepared through two methods: the conventional impregnation method (denoted as M-TiO_2(IM)) and the *in situ* hydrothermal loading method (denoted as M-TiO_2(HT)). In the impregnation method, $RuCl_3$ and H_2IrCl_6 were used as precursors. Pure TiO_2 nanosheets powder was impregnated in an aqueous solution containing a given amount of the chloride salts (the amount of RuO_2 and IrO_2 is 0.5 wt %). The solution was then evaporated over a water bath at 50 °C followed by a calcination in air at 300 °C for 1 h. The specific surface areas of Ru-TiO_2(IM) and Ir-TiO_2(IM) are 90.5 and 95.0 m^2/g tested by N_2 absorption−desorption isotherms. In the *in situ* loading method, similar to the TM-TiO_2 nanosheets, $RuCl_3$ (0.45g) and H_2IrCl_6 (0.75g) were used as precursors. The specific surface areas of Ru-TiO_2(HT) and Ir-TiO_2(HT) were 93.5 and 97.0 m^2/g as tested by N_2 absorption−desorption isotherms.

Characterization. X-ray diffraction (XRD) measurement patterns were recorded on a Philips X'pert Pro diffractometer using Ni-filtered Cu Kα1 radiation (λ = 0.15 nm). The X-ray tube was operated at 40 kV and 40 mA.

Transmission electron microscopy (TEM) images were taken on a JEM-2100 instrument at an acceleration voltage of 200 kV. The samples were crushed and dispersed in A.R. grade ethanol, and the resulting suspensions were allowed to dry on carbon film supported on copper grids. Scanning transmission electron microscopy (STEM) images were taken on a high resolution transmission electron microscopy instrument (FEI TECNAI F20) with HAADF detector operator at 300 kV.

X-ray fluorescence (XRF) spectroscopy analysis was operated on a ARL ADVANT'X instrument, using Rh Kα radiation operating at 3600 W. The X-ray tube was operated at 60 kV and 120 mA.

X-ray photoelectron spectroscopy (XPS) analysis was performed on a PHI 5000 VersaProbe system, using monochromatic Al Kα radiation (1486.6 eV) operating at 25 W. The sample was outgassed overnight at room temperature in a UHV chamber ($<5 \times 10^{-7}$ Pa). All binding energies (BE) were referenced to the C 1s peak at 284.6 eV. The experimental errors were within ±0.1 eV.

dx.doi.org/10.1021/cs4002755 | ACS Catal. 2013, 3, 2052−2061

UV−vis diffuse reflectance spectroscopy (UV−vis DRS) were recorded in the range of 200−900 nm on a Shimadzu UV-2401 spectrophotometer with $BaSO_4$ as reference.

Time-resolved PL fluorescence spectra of the solution were obtained using a FLS920 spectrometer (Edinburgh Instruments). The excitation wavelength is 350 nm, and the probe wavelength is 468 nm.

Photocatalytic Reaction. The O_2 evolution reactions were performed in a Pyrex top-irradiation reaction vessel connected to a glass closed gas circulation system at room temperature; 0.1 g of the as-prepared sample was dispersed in 100 mL of 0.02 M aqueous $NaIO_3$ solution (potassium phosphate buffer solution, pH ≈ 6.9) unless otherwise stated. The reactant solution was evacuated several times to ensure complete air removal, followed by the introduction of argon into the system. The reaction was initiated by irradiation with a 150 W UV lamp. The evolved gases were analyzed by an online gas chromatograph (Shimadzu with TCD detector and MS-5A column, argon carrier gas).

The apparent quantum efficiency (QE) was measured under the same photocatalytic reaction conditions. Four low power UV-LEDs (5 W, 365 nm), which were positioned 1 cm away from the reactor in four different directions, were used as light sources to trigger the photocatalytic reaction. The focused intensity and areas on the flask for each UV-LED was ca. 120 mW/cm^2 and 1 cm^2, respectively. The QE was measured and calculated according to the following equation:

$$\mathrm{QE}\ (\%) = \frac{\text{no. of reacted electrons}}{\text{no. of reacted electrons}} \times 100$$

$$= \frac{2 \times \text{no. of evolved } H_2 \text{ molecules}}{\text{no. of incident photons}} \times 100$$

Photoelectrochemical Measurements. Photocurrent was measured on an electrochemical analyzer (CHI660C Instruments) in a standard three-electrode system using the prepared samples as the working electrodes with an active area of ca. 1.0 cm^2, a Pt wire as the counter electrode, and Ag/AgCl (saturated KCl) as a reference electrode. A low power UV-LED (3 W, 365 nm) was used as a light source, and 0.5 M Na_2SO_4 aqueous solution was employed as the electrolyte. The working electrodes were prepared as follows: 0.15 g of the sample was ground with 0.06 g poly(ethylene glycol) (PEG, molecular weight 20,000) and 0.5 mL ethanol to make a slurry. Then, the slurry was coated onto a 2 cm × 1.2 cm F-doped SnO_2-coated glass (FTO glass) electrode by the doctor blade technique. Next, these electrodes were dried in an oven and calcinated at 300 °C for 30 min. All investigated electrodes have a similar film thickness.

RESULTS AND DISCUSSIONS

The XRD patterns of TM are shown in Figure 1. All of these samples show the typical diffraction patterns of anatase TiO_2 (JCPDS no. 21-1272) without any other peaks. After comparing the position and intensity of the diffraction peaks in TiO_2 nanosheets modified with different metal oxides, we can find that different ions show negligible influences on the phase structures on TM-TiO_2 samples. No ions have been doped into the framework of TiO_2 crystal lattice. Furthermore, no other peaks corresponding to other metal oxides can be found in Figure 1, and it is inferred that these transition metal oxides (e.g., Mn, Fe, Co, Ni and Cu) exist as clusters whose sizes are beyond the detection limit of XRD (~3 nm). In order

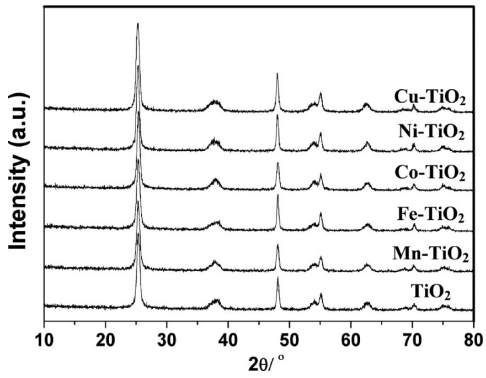

Figure 1. XRD patterns of pure TiO_2 nanosheets and TM-TiO_2 nanosheets.

to further investigate the surface structures of TM-TiO_2 nanosheets, Raman spectra are also tested. As shown in Supplementary Figure S1, these samples show similar Raman signals, in both the position of the peaks and their intensity. To further investigate the distribution of transition metal elements, we have washed TiO_2 nanosheets with 0.2 M aqueous HNO_3 to remove the surface TM clusters. XRF analysis indicates that no TM elements are residual in the treated samples, suggesting that metal ions have not doped into the TiO_2 lattice.

XRD and Raman spectra have proved that the TM-TiO_2 nanosheets exhibit the same crystal structures as pure TiO_2 nanosheets. Transmission electron microscopy (TEM) analysis is performed to characterize their morphology features. From Figure 2, we can observe that pure TiO_2 nanosheets are composed of rectangular nanosheets with side length of ca. 20−70 nm and thickness of ca. 4−8 nm. As for TM-TiO_2 samples, the main ingredients are also TiO_2 nanosheets with similar sizes compared with pure TiO_2 nanosheets. High-resolution transmission electron microscopy (HRTEM) images are shown in Supplementary Figure S2. The lattice spacing parallel to the top and bottom facets is ~0.235 nm, corresponding to the {001} planes of anatase TiO_2.[23] The TM-TiO_2 samples show similar morphology compared with that of pure TiO_2, indicating the addition of other metal ions does not impact the growth of TiO_2 nanosheets.

Notably, there are many small clusters dispersed on the TiO_2 nanosheets in the TM-TiO_2 samples. In our previous study, we have proved that these ultrasmall oxide particles are amorphous phase and have intimate contact with TiO_2 nanosheets.[24] Scanning transmission electron microscopy (STEM) is used to further observe the metal oxide clusters dispersed on TiO_2 nanosheets. The STEM images are displayed in Figure 3. The pure TiO_2 nanosheets exhibit a smooth surface, while the TM-TiO_2 samples show a rough surface with many clusters as small as ~2 nm. The size distributions of these metal oxide clusters are summarized in Supplementary Figure S3. We can find out that the sizes of metal oxide clusters in different samples are quite similar. These clusters can be easily differentiated from the support (TiO_2 nanosheets). In our previous work, an *in situ* TEM experiment was carried out to identify the component of the amorphous particles.[24] In the Cu-TiO_2 sample, the lattice fringes corresponding to metallic Cu appear after e-beam irradiation. This experiment suggests that these amorphous particles are made up of transition metal oxides. Since the hydrothermal reaction is performed in an acid environment (HF), TiO_2 will form at first due to its fast reaction with aqueous HF. The metal salts ($Cu(Ac)_2$, etc.) will hydrolyze

dx.doi.org/10.1021/cs4002755 | ACS Catal. 2013, 3, 2052−2061

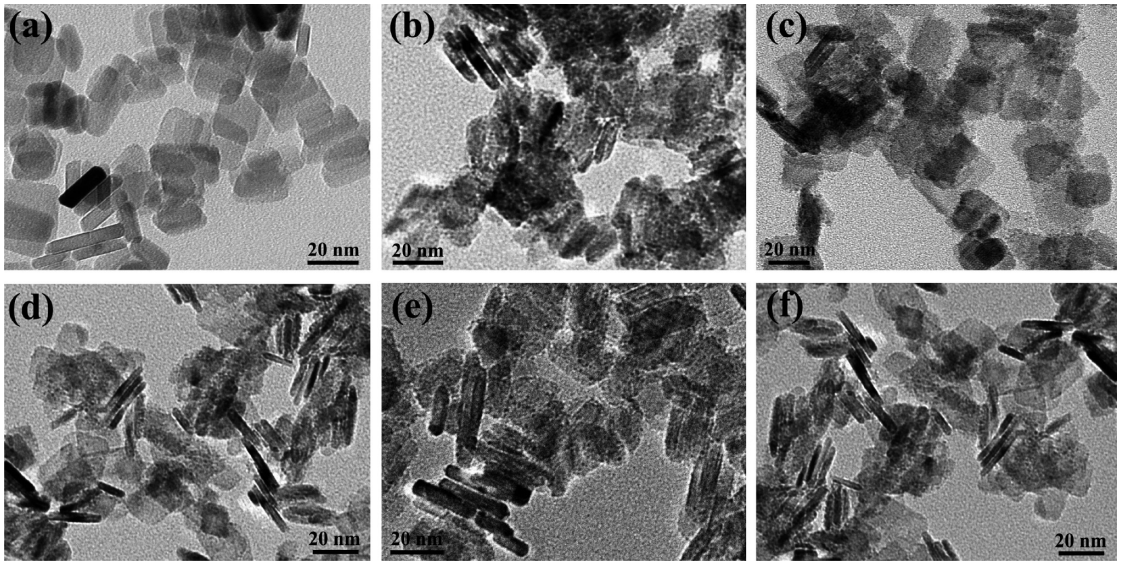

Figure 2. TEM images of pure TiO_2 nanosheets and TM-TiO_2 nanosheets: (a) TiO_2, (b) Mn-TiO_2, (c) Fe-TiO_2, (d) Co-TiO_2, (e) Ni-TiO_2, and (f) Cu-TiO_2.

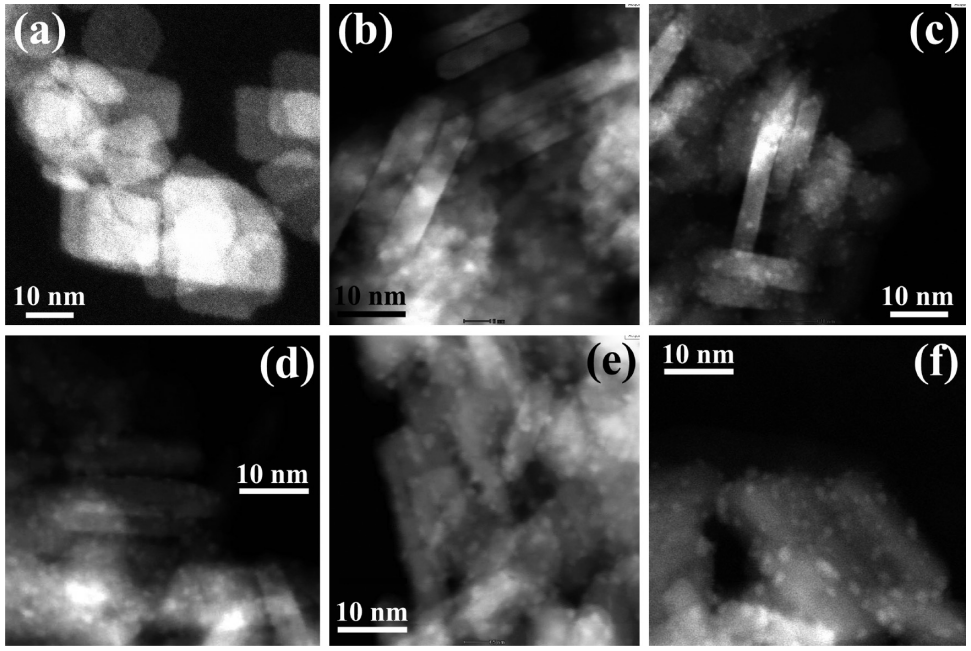

Figure 3. STEM images of pure TiO_2 nanosheets and TM-TiO_2 nanosheets: (a) TiO_2, (b) Mn-TiO_2, (c) Fe-TiO_2, (d) Co-TiO_2, (e) Ni-TiO_2, and (f) Cu-TiO_2.

after the consumption of HF, resulting in the formation of metal oxide clusters on TiO_2 nanosheets. On the basis of the above analysis, we can conclude that TiO_2 nanosheets modified with metal oxide clusters can be prepared through the *in situ* loading method.

The amounts of transition metal oxides in the TM-TiO_2 samples are measured by XRF. As listed in Table 1, the contents of metal oxides range from 0.45% to 0.55%. The XPS spectra of TM-TiO_2 samples are also tested, as displayed in Figure 4. After comparing the banding energy of the peaks with standard spectra, we can identify the chemical status and amounts of the metal oxide species on TiO_2 nanosheets.[25] According to previous literature, on the basis of the binding energy of the peaks in the 2p region, S/M ratio (satellite intensity/main peak intensity), and the spin−orbit coupling

Table 1. Relative Atomic Ratios of Various Elements in Pure TiO_2 Nanosheets and TM-TiO_2 Nanosheets Measured by XPS

sample	Ti (%)	O (%)	metal (%)
TiO_2 nanosheets	30.12	69.87	
Mn-TiO_2	29.32	68.70	1.48
Fe-TiO_2	29.40	69.09	1.51
Co-TiO_2	29.30	69.15	1.55
Ni-TiO_2	29.64	68.88	1.48
Cu-TiO_2	29.57	69.08	1.50

DE, the main components of the metal oxides supported on TiO_2 nanosheets are ascribed to MnO,[26] Fe_2O_3,[27] Co_3O_4,[28,29] NiO,[30] and Cu_2O.[31] It should be pointed out that the above

dx.doi.org/10.1021/cs4002755 | *ACS Catal.* 2013, 3, 2052−2061

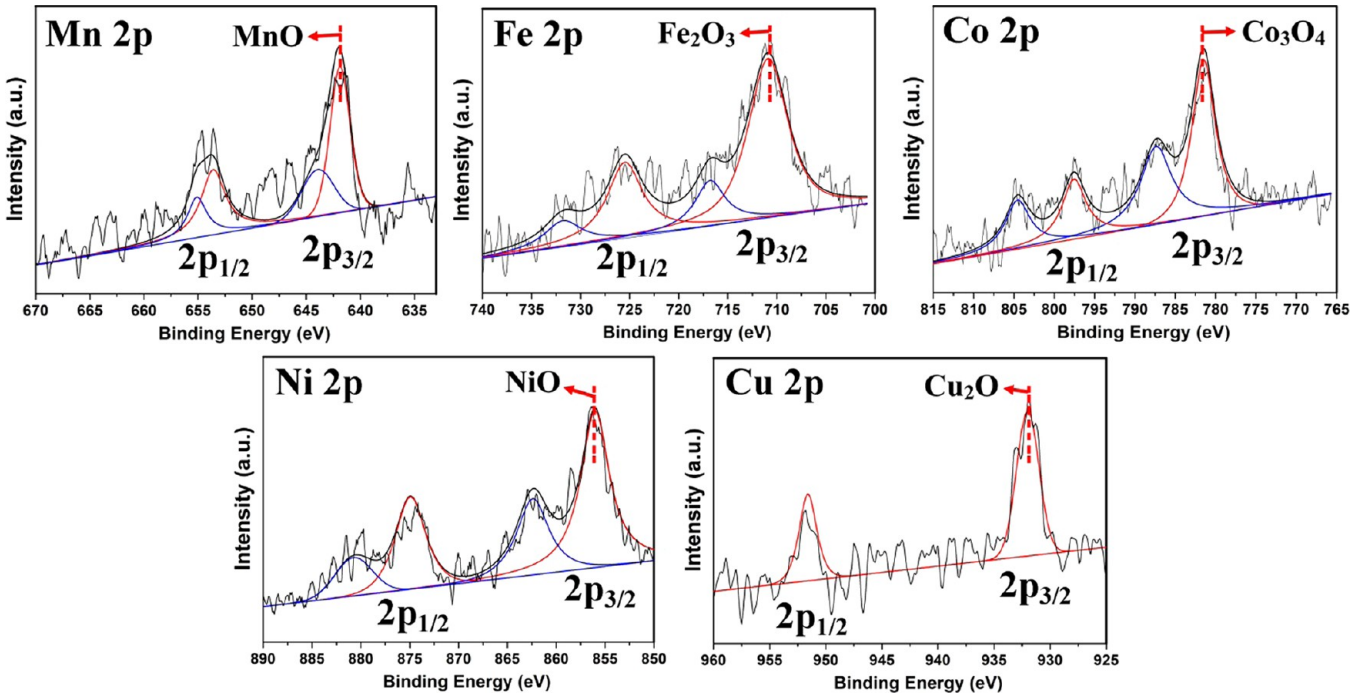

Figure 4. XPS spectra of TM-TiO_2 nanosheets.

ascriptions are only qualitative due to the complexity of the surface of TiO_2 nanosheets. Some mixed-valence states may exist in these metal oxide clusters, especially for Co and Mn because their chemical status is hard to distinguish by XPS. The results of the XPS analysis are summarized in Table 2. The

Table 2. Relative Atomic Ratios of Various Elements in Pure TiO_2 Nanosheets and TM-TiO_2 Nanosheets Measured by XRF

sample	Ti (%)	O (%)	metal (%)
TiO_2 nanosheets	33.33	66.67	
Mn-TiO_2	33.70	66.51	0.49
Fe-TiO_2	33.11	66.39	0.50
Co-TiO_2	32.95	66.55	0.55
Ni-TiO_2	32.85	66.65	0.52
Cu-TiO_2	33.03	66.62	0.55

amounts of transition metal elements obtained from XPS are much larger than those obtained from XRF, which implies an enrichment of transition metal elements on the surface and is consistent with the TEM and STEM analysis.

The effects of metal oxide clusters loading on the pore structure and surface areas of as-prepared TM-TiO_2 samples are investigated by N_2 adsorption−desorption. It can be seen from Figure 5a that all of these samples show isotherms of type IV according to the Brunauer−Deming−Deming−Teller (BDDT) classification, indicating the presence of mesopores (2−50 nm).[32] The corresponding hysteresis loops are type H3 at a high relative pressure range of 0.75−1.0, suggesting the presence of slit-like pores.[33] The generation of hysteresis loops is from the aggregation of the sheet-like TiO_2 nanoparticles. If we compare these hysteresis loops carefully, we can find that the TM-TiO_2 samples show relatively narrow hysteresis loops located at 0.8−0.9. This difference can also be reflected in the pore size distributions of TiO_2 and TM-TiO_2 samples (Figure 5b). Obviously, in TM-TiO_2 all of them show

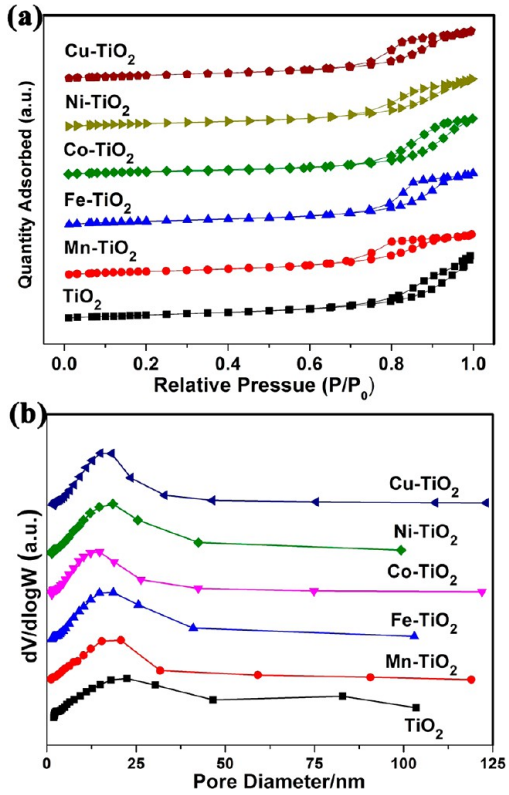

Figure 5. (a) N_2 absorption−desorption isotherms of pure TiO_2 nanosheets and TM-TiO_2 nanosheets. (b) Pore size distributions of pure TiO_2 nanosheets and TM-TiO_2 nanosheets.

narrow size distributions with an average pore size between 15 and 20 nm. As for pure TiO_2 nanosheets, they show a wider size distribution compared to TM-TiO_2 samples and a larger average pore size of 20.5 nm. The BET surface area and pore volume for these samples are listed in Table 3.

dx.doi.org/10.1021/cs4002755 | ACS Catal. 2013, 3, 2052−2061

Table 3. BET Surface Area, Pore Volume, and Average Pore Sizes of TiO_2 Nanosheets and TM-TiO_2 Nanosheets

sample	S_{BET} (m^2/g)	pore volume (cm^3/g)	av pore size (nm)
TiO_2 nanosheets	104	0.30	20.5
Mn-TiO_2	94	0.28	17.0
Fe-TiO_2	98	0.28	16.7
Co-TiO_2	98	0.28	15.2
Ni-TiO_2	100	0.29	16
Cu-TiO_2	99	0.28	15.6

The photoabsorption properties are very important to photocatalytic materials. UV−vis spectra of TM-TiO_2 nanosheets and pure TiO_2 nanosheets are shown in Figure 6. Pure TiO_2 nanosheets show only UV absorption with a cutoff wavelength at 400 nm due to the large band gap. When transition metal oxide clusters are loaded on TiO_2 nanosheets, some new peaks appear. They are corresponding to their band gap absorption of metal oxide clusters and d-d transition of Fe, Co, Ni, and Cu. Because of d^5 electron structure of Mn^{2+}, Mn-TiO_2 shows a similar UV−vis absorption as pure TiO_2.[34] The cutoff wavelengths of the TM-TiO_2 samples are also fingered out in Figure 6. Notably, all of these samples show cutoff wavelengths located at 394−399 nm, which is the same as for pure TiO_2 nanosheets. This indicates that the band structures of TM-TiO_2 do not change after loading metal oxide clusters. If metal ions are doped into the framework of the TiO_2 lattice, the cutoff wavelength will show a red or blue shift compared to pure TiO_2 nanosheets. However, no blue or red shift of the cutoff wavelength can be observed. On the other hand, this phenomenon also confirms the heterojunction structures of TM-TiO_2 nanosheets obtained according to the TEM and STEM images. Since a UV light source (output light is around 365 nm, and the percentage of output light in visible range (>420 nm) is lower than 10%) is used in the photocatalytic tests, TiO_2 nanosheets with large absorption in the UV region will play the dominate roles in harvesting UV light. Because the intrinsic band of TiO_2 nanosheets are preserved after loading transition metal oxide clusters, the effects of metal oxide clusters will be shown in the stage of electron−hole separation.

In this work, we have prepared RuO_2/TiO_2 and IrO_2/TiO_2 nanosheets through two methods (conventional impregnation, denoted as M-TiO_2(IM) and the in situ loading by hydrothermal reactions, denoted as M/TiO_2(HT)) for comparison. The morphological information about these samples is presented in Supplementary Figures S4 and S5. Notably, the size of RuO_2 and IrO_2 clusters in the MO_2-TiO_2(IM) samples are as large as 5 nm, whereas ultrasmall RuO_2 and IrO_2 clusters (~2 nm) are formed on TiO_2 nanosheets through *in situ* loading, implying their different photoactivities. The big difference in the particle size can be ascribed to the controllable precipitation and deposition of $RuCl_3$ and H_2IrCl_6 during hydrothermal reaction.[24]

Since the charge separation and interface charge-transfer process are ultrafast, we employ time-resolved PL spectra to further reveal the relationships between their structures and photoactivities for TM-TiO_2 and other samples. The PL signal intensity will decay after a 350 nm laser pulse excitation. Samples with efficient charge separation will show a slow PL signal decay due to the long lifetime of photogenerated holes and electrons.[35,36] As we can see in Figure 7 and the corresponding fitting results in Table 4, pure TiO_2 nanosheets show the shortest decay time due to low efficiency in electron−hole separation. After loading co-catalysts, the photogenerated electrons and holes will separate through interface charge transfer, leading to a longer lifetime of the PL signal. Ru-TiO_2(IM) shows a slower PL intensity decay compared to that of pure TiO_2 nanosheets, suggesting the promotion effect of RuO_2 nanoparticles as co-catalysts. Moreover, Ru-TiO_2(HT) shows a longer decay time compared with that of Ru-TiO_2(IM), indicating the importance of size effect of RuO_2 co-catalysts. As for TM-TiO_2 samples, the decay times are obviously increase compared to that of pure TiO_2 nanosheets.

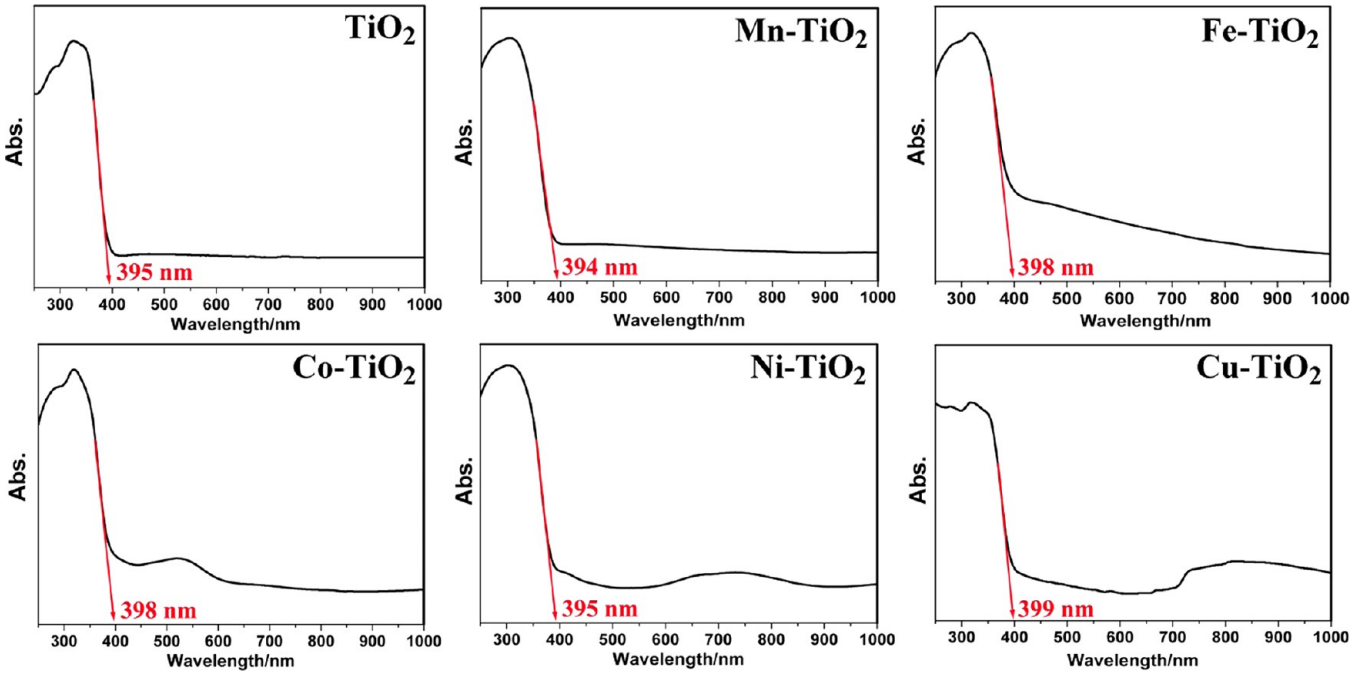

Figure 6. UV−vis diffuse reflectance spectra of pure TiO_2 sheets and TM-TiO_2 nanosheets.

dx.doi.org/10.1021/cs4002755 | *ACS Catal.* 2013, 3, 2052−2061

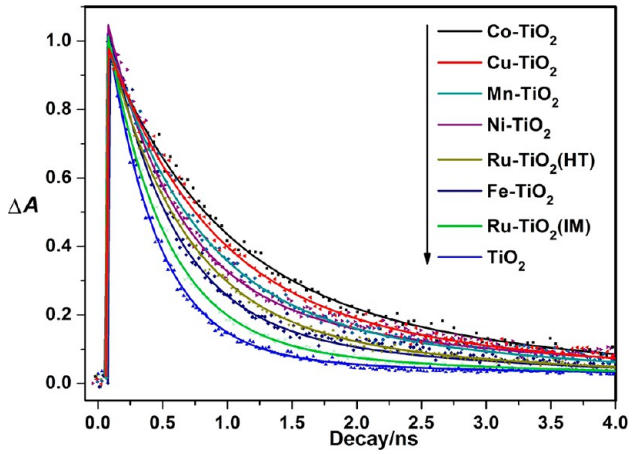

Figure 7. Time-resolved PL spectra of pure TiO_2 nanosheets and Ru-TiO_2(IM), Ru-TiO_2-(HT), and TM-TiO_2 nanosheets.

Table 4. Fitting Parameters of Time-Resolved PL Spectra of TiO_2 Nanosheets and Ru-TiO_2(IM), Ru-TiO_2(HT), and TM-TiO_2 Nanosheets

	decay (ns)	
sample	τ_1	τ_2
TiO_2 nanosheets	0.35	2.39
Ru-TiO_2(IM)	0.40	2.60
Ru-TiO_2(HT)	0.50	2.84
Mn-TiO_2	0.65	3.20
Fe-TiO_2	0.43	2.78
Co-TiO_2	0.85	4.20
Ni-TiO_2	0.58	3.10
Cu-TiO_2	0.75	3.85

In particular, Co-TiO_2, Cu-TiO_2, and Mn-TiO_2 show relatively slower PL intensity decay among the eight samples, indicating their highly efficient electron−hole separation.

To investigate the effects of loading metal oxide clusters on TiO_2 nanosheets, we employ the photocatalytic O_2 evolution from water as a probe reaction to test the promotion effect of metal oxide clusters. The O_2 evolution rates of different samples are shown in Figure 8a. As for a pure TiO_2 sample, the O_2 evolution rate is trace, indicating the important roles of co-catalysts. After loading RuO_2 and IrO_2 by impregnation as co-catalysts, the O_2 evolution rates are improved to 18.2 and 15.7 μmol·h^{-1}. Furthermore, O_2 evolution rates increase to 36.5 and 30.5 μmol·h^{-1}. As for the TM-TiO_2 nanosheets, O_2 evolution rates are significantly promoted compared to those of Ru-TiO_2(IM) and Ir-TiO_2(IM). Mn-TiO_2 and Co-TiO_2 show the best activity, which are almost 3-fold that of Ir-TiO_2(IM). The O_2 evolution rate of Co-TiO_2 is as high as 47 μmol·h^{-1}. Although the sizes of RuO_2 and IrO_2 clusters in Ru-TiO_2(IM) and Ir-TiO_2(IM) are similar to those in TM-TiO_2, the O_2 evolution rates of Co-TiO_2 and Mn-TiO_2 are still much higher. The apparent quantum yields of Co-TiO_2 and Mn-TiO_2 are 15.5% and 13.9%, respectively. Compared to some similar works, they show excellent performances in a water oxidation reaction.[37,38] Ni-TiO_2 and Fe-TiO_2 show relatively lower O_2 evolution rates compared with those of Mn-TiO_2 and Co-TiO_2. It is notable that the Cu-TiO_2 sample shows poor activity in O_2 evolution, which is a drastic contrast with other TM-TiO_2 samples. A schematic illustration of the mechanism for the photocatalytic water oxidation by TM-TiO_2 samples are shown in Figure 8b. When TiO_2 nanosheets absorb UV light, electrons are excited to the conduct band of TiO_2, leaving holes in the valence band. The photogenerated holes will move to the metal oxide clusters through interface charge transfer,[7,39,40] resulting in the separation of electrons and holes. Subsequently, the active holes will oxidize H_2O or OH^- to O_2.

In the photocatalytic reactions, two crucial factors will affect the activity: the charge separation efficiency and reactivity of photogenerated holes. The time-resolved PL spectra have shown that the charge-transfer rates in different catalysts are distinct. Co-TiO_2, Cu-TiO_2, and Mn-TiO_2 show relative fast charge transfer across the metal oxide clusters−TiO_2 nanosheets heterojunctions. Furthermore, after separation, the potential of photogenerated holes at the metal oxide clusters will also affect the O_2 evolution activity. The bottoms of the valence band for transition metal oxide clusters are higher than that of TiO_2 (the band structures of TiO_2 and transition metal oxides are presented in Supplementary Figure S6).[41] In Supplementary Figure S6, we can figure out that the bottom of the conduct band of Cu_2O is higher than the potential of O_2/H_2O. When the photogenerated holes transfer to Cu_2O, they do not have enough energy to oxidize H_2O to O_2, leading to the poor activity,[17] although the charge separation efficiency is higher than for other TM-TiO_2 samples (as proved by PL spectra). Because of their advantages in fast interface charge transfer and highly active holes, Co-TiO_2 and Mn-TiO_2 show excellent performance in water photocatalytic oxidation to O_2. The relatively lower efficiency in interface charge transfer of Ni-TiO_2 and Fe_2O_3 result in their low O_2 evolution rates compared with those of Mn-TiO_2 and Co-TiO_2.

On the basis of the above activity test and time-resolved PL spectra, we can find that the promotion effects of metal oxide clusters on photoactivity of TiO_2 nanosheets are quite evident. Transient photocurrent responses of pure TiO_2 nanosheets, Ru-TiO_2 nanosheets, and Co-TiO_2 nanosheets are shown in Figure 9. The Ru-TiO_2 shows current density higher than that of pure TiO_2 nanosheets, suggesting the higher charge separation efficiency in Ru-TiO_2.[42,43] When CoO_x clusters are loaded on TiO_2 as co-catalysts, the current density is improved significantly, which is consistent with the high O_2 evolution rate of the Co-TiO_2 sample.

We have also optimized the amount of metal oxide clusters. As shown in Figure 10a, When the content of CoO_x is lower than 0.55 wt %, the O_2 evolution rate grows with the increase of CoO_x loading amount. Further increasing the amount of CoO_x will cause a drop in O_2 evolution rate. When the amount of CoO_x is as high as 2 wt %, Co-TiO_2 almost loses its activity in photocatalytic O_2 evolution. In our previous work, we have found the size of metal oxide particles will grow to as large as 3−4 nm with the increase of loading amount.[24] Since the electronic structures of semiconductors are closely related to their sizes,[44,45] the electronic structures of heterojunctions between metal clusters and TiO_2 nanosheets also depend on the size of metal clusters. When the size of CoO_x particles is larger than 3 nm, the charge transfer between CoO_x and TiO_2 nanosheets will decline acutely, leading to a drop in photocatalytic activity. On the other hand, through the one-pot reaction, metal oxide clusters can be *in situ* loaded on TiO_2 nanosheets with controllable sizes, which is a facile method to enhance the photoactivity. The stability of Co-TiO_2 nanosheets was also tested. As shown in Figure 10b, after 5 cycles, the O_2 evolution rate still achieves 44 μmol·h^{-1}. Besides, the morphology of Co-TiO_2 is preserved after 5 cycles with

dx.doi.org/10.1021/cs4002755 | *ACS Catal.* 2013, 3, 2052−2061

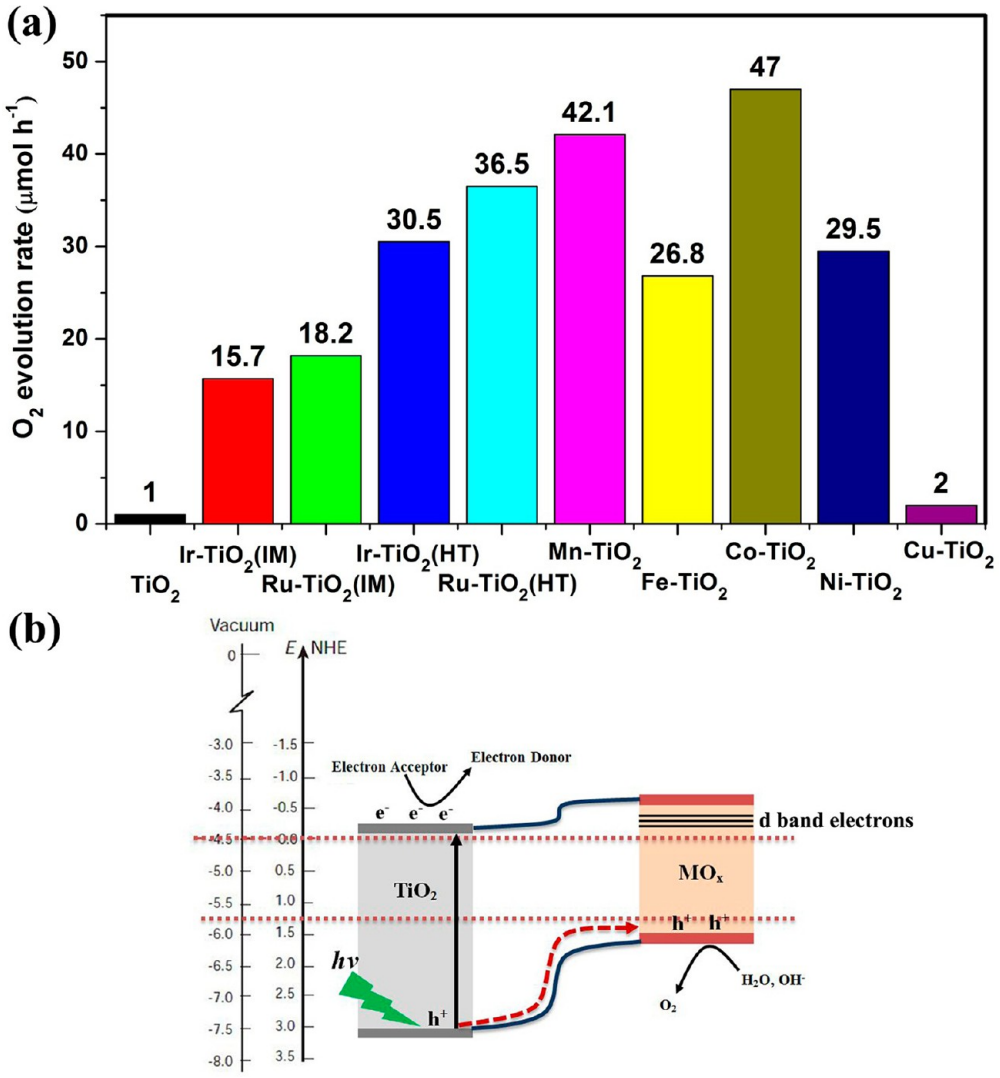

Figure 8. (a) O_2 evolution rates of different catalysts. (b) Schematic diagram of photocatalytic water oxidation to O_2 by TiO_2 nanosheets with metal oxide clusters.

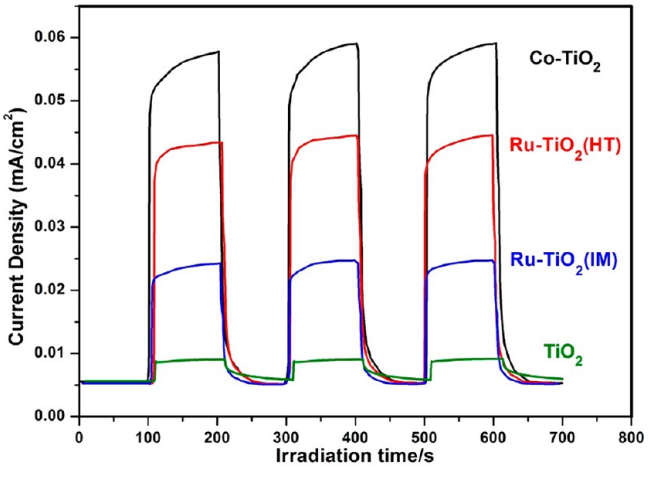

Figure 9. Transient photocurrent responses of pure TiO_2 nanosheets and Ru-TiO_2(IM), Ru-TIO_2(HT), and Co-TiO_2 nanosheets under UV irradiation at 0.5 V versus Ag/AgCl.

CoO_x metal clusters dispersed on TiO_2 nanosheets (Supplementary Figure S7). The above experiments prove that TiO_2 nanosheets modified with metal oxide clusters are stable photocatalysts.

CONCLUSION

In this work, a facile one-pot method was developed for in situ loading of transition metal oxide clusters on TiO_2 nanosheets. These clusters with a size of ~2 nm are finely dispersed on TiO_2 nanosheets. Heterojunctions are formed between TiO_2 nanosheets and the modified metal oxide clusters, favoring charge transfer across the interface. Under UV light excitation, photogenerated holes can move from TiO_2 to metal oxide clusters, leading to separation of electrons and holes. These transition metal oxide clusters can serve as co-catalysts to trap photogenerated holes and participate in photocatalysis. Photocatalytic O_2 evolution from water was used to test the photoactivity of TM-TiO_2 samples. Due to the higher charge separation efficiency, TM-TiO_2 samples showed much better performances compared with that of pure TiO_2 nanosheets, Ru-TiO_2, and Ir-TiO_2. These results suggest that transition metal oxide clusters with small sizes can be promising substitutes for noble metal oxides (RuO_2, IrO_2) as co-catalysts in photo-

dx.doi.org/10.1021/cs4002755 | ACS Catal. 2013, 3, 2052−2061

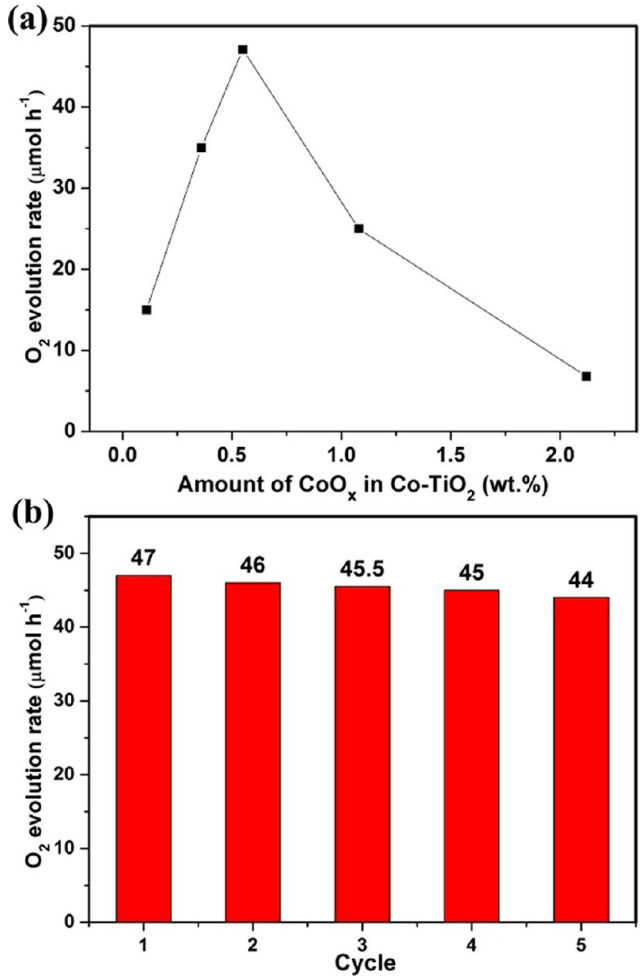

Figure 10. (a) O_2 evolution rates of Co-TiO_2 with different amounts of CoO_x. (b) Cyclability of Co-TiO_2 in photocatalytic O_2 evolution from water oxidation.

catalysis and may serve as more economic and active photocatalysts.

■ ASSOCIATED CONTENT

Supporting Information

Additional experimental results including the structural characterizations, band gap scheme, and other data. This material is available free of charge via the Internet at http://pubs.acs.org.

■ AUTHOR INFORMATION

Corresponding Author

*Tel.: +86 25 83592290. Fax: +86 25 83317761. E-mail: tangcj@nju.edu.cn (C.T.); donglin@nju.edu.cn (L.D.).

Notes

The authors declare no competing financial interest.

■ ACKNOWLEDGMENTS

The financial supports of the National Nature Science Foundation of China (no. 21203091), Natural Science Foundation of Jiangsu Province (BK2012298), the National 973 Program of China (no. 2010CB732300), and National Undergraduate Innovation Program (XZ101028426) were gratefully acknowledged.

■ REFERENCES

(1) Chen, X.; Shen, S.; Guo, L.; Mao, S. S. *Chem. Rev.* **2010**, *110*, 6503.
(2) Fujishima, A.; X. Zhang, X.; Tryk, A. D. *Surf. Sci. Rep.* **2008**, *63*, 515.
(3) Asahi, R.; Morikawa, T.; Ohwaki, T.; Aoki, K.; Taga, Y. *Science* **2001**, *293*, 269.
(4) Liu, G.; Yin, L.-C.; Wang, J.; Niu, P.; Zhen, C.; Xie, Y.; Cheng, H.-M. *Energy Environ. Sci.* **2012**, *5*, 9603.
(5) Etgar, L.; Gao, P.; Xue, Z.; Peng, Q.; Chandiran, A. K.; Liu, B.; Nazeeruddin, M. K.; Gratzel, M. *J. Am. Chem. Soc.* **2012**, *134*, 17396.
(6) Kongkanand, A.; Tvrdy, K.; Takechi, K.; Kuno, M.; Kamat, P. V. *J. Am. Chem. Soc.* **2008**, *130*, 4007.
(7) Kamat, P. V. *J. Phys. Chem. Lett.* **2012**, *3*, 663.
(8) Jang, J. S.; Kim, H. G.; Lee, J. S. *Catal. Today* **2012**, *185*, 270.
(9) Chen, X. B.; Shen, S. H.; Guo, L. J.; Mao, S. S. *Chem. Rev.* **2010**, *110*, 6503.
(10) Lin, F.; Wang, D.; Jiang, Z.; Ma, Y.; Li, J.; Li, R.; Li, C. *Energy Environ. Sci.* **2012**, *5*, 6400.
(11) Li, K.; Chai, B.; Peng, T.; Mao, J.; Zan, L. *ACS Catal.* **2013**, *3*, 170.
(12) Ma, Y.; Xu, Q.; Zong, X.; Wang, D.; Wu, G.; Wang, X.; Li, C. *Energy Environ. Sci.* **2012**, *5*, 6345.
(13) Tanaka, A.; Sakaguchi, S.; Hashimoto, K.; Kominami, H. *ACS Catal.* **2013**, *3*, 79.
(14) Liu, M.; Qiu, X.; Miyauchi, M.; Hashimoto, K. *J. Am. Chem. Soc.* **2013**, *135*, 10064.
(15) Meekins, B. H.; Kamat, P. V. *J. Phys. Chem. Lett.* **2011**, 2304.
(16) Lin, F.; Zhang, Y.; Wang, L.; Zhang, Y.; Wang, D.; Yang, M.; Yang, J.; Zhang, B.; Jiang, Z.; Li, C. *Appl. Catal. B: Environ.* **2012**, *127*, 363.
(17) Maeda, K.; Domen, K. *J. Phys. Chem. Lett.* **2010**, *1*, 2655.
(18) Long, M.; Cai, W.; Cai, J.; Zhou, B.; Chai, X.; Wu, Y. *J. Phys. Chem. B* **2006**, *110*, 20211.
(19) Zhang, F.; Yamakata, A.; Maeda, K.; Moriya, Y.; Takata, T.; Kubota, J.; Teshima, K.; Oishi, S.; Domen, K. *J. Am. Chem. Soc.* **2012**, *134*, 8348.
(20) Townsend, T. K.; Browning, N. D.; Osterloh, F. E. *ACS Nano* **2012**, *6*, 7420.
(21) Townsend, T. K.; Browning, N. D.; Osterloh, F. E. *Energy Environ. Sci.* **2012**, *5*, 9543.
(22) Tisdale, W. A.; Williams, K. J.; Timp, B. A.; Norris, D. J.; Aydil, E. S.; Zhu, X. Y. *Science* **2010**, *328*, 1543.
(23) Han, X.; Kuang, Q.; Jin, M.; Xie, Z.; Zheng, L. *J. Am. Chem. Soc.* **2009**, *131*, 3152.
(24) Liu, L.; Gu, X.; Sun, C.; Li, H.; Deng, Y.; Gao, F.; Dong, L. *Nanoscale* **2012**, *4*, 6351.
(25) Moulder, J. F.; Stickle, W. F.; Sobol, P. E.; Bomben, K. D. *Handbook of X-ray Photoelectron Spectroscopy*, Perkin-Elmer Corp.: Waltham, MA, 1992.
(26) Li, D.; Yu, Q.; Li, S.-S.; Wan, H.-Q.; Liu, L.-J.; Qi, L.; Liu, B.; Gao, F.; Dong, L.; Chen, Y. *Chem.—Eur. J.* **2011**, *17*, 5668.
(27) Yamashita, T.; Hayes, P. *Appl. Surf. Sci.* **2008**, *254*, 2441.
(28) Lv, Y.; Zhang, H.; Cao, Y.; Dong, L.; Zhang, L.; Yao, K.; Gao, F.; Chen, Y. *J. Colloid Interface Sci.* **2012**, *372*, 63.
(29) Lv, Y.; Liu, L.; Zhang, H.; Yao, X.; Gao, F.; Yao, K.; Dong, L.; Chen, Y. *J. Colloid Interface Sci.* **2013**, *390*, 158.
(30) Peck, M. A.; Langell, M. A. *Chem. Mater.* **2012**, *24*, 4483.
(31) Sun, C.; Zhu, J.; Lv, Y.; Qi, L.; Liu, B.; Gao, F.; Sun, K.; Dong, L.; Chen, Y. *Appl. Catal. B: Environ.* **2011**, *103*, 206.
(32) Sun, C.; Liu, L.; Qi, L.; Li, H.; Zhang, H.; Li, C.; Gao, F.; Dong, L. *J. Colloid Interface Sci.* **2011**, *364*, 288.
(33) Lv, K.; Xiang, Q.; Yu, J. *Appl. Catal. B: Environ.* **2011**, *104*, 275–281.
(34) Cotton, F. A.; Wilkinson, G.; Murillo, C. A.; Bochmann, M. *Advanced Inorganic Chemistry*, 6th ed.; Wiley: New York,1999.
(35) Shi, J.; Chen, J.; Feng, Z.; Chen, T.; Wang, X.; Ying, P.; Li, C. *J. Phys. Chem. B* **2006**, *110*, 25612.
(36) Thompson, T. L.; Yates, J. T., Jr. *Chem. Rev.* **2006**, *106*, 4428.

(37) Zhang, L.; Xu, L.; Wang, J.; Shao, H.; Fan, Y.; Zhang, J. *J. Phys. Chem. C* **2011**, *115*, 18027.
(38) Abe, R.; Sayama, K.; Sugihara, H. *J. Phys. Chem. B* **2005**, *109*, 16052.
(39) Zhang, Z.; Shao, C.; Li, X.; Wang, C.; Zhang, M.; Liu, Y. *ACS Appl. Mater. Interfaces* **2010**, *2*, 2915.
(40) Cao, T.; Li, Y.; Wang, C.; Shao, C.; Liu, Y. *Langmuir* **2011**, *27*, 2946.
(41) Gratzel, M. *Nature* **2001**, *414*, 338.
(42) Zhong, D. K.; Choi, S.; Gamelin, D. R. *J. Am. Chem. Soc.* **2011**, *133*, 18370.
(43) Kongkanand, A.; Tvrdy, K.; Takechi, K.; Kuno, M.; Kamat, P. V. *J. Am. Chem. Soc.* **2008**, *130*, 4007.
(44) Rossetti, R.; Ellison, J. L.; Gibson, J. M.; Brus, L. E. *J. Chem. Phys.* **1984**, *80*, 4464.
(45) Brus, L. E. *J. Chem. Phys.* **1984**, *80*, 4403.